

Er³⁺/Yb³⁺-Doped GdVO₄ Obtained by the Non-Hydrolytic Sol-Gel Route and Potential Application as Up-Conversion Thermometer

Maria F. Ferreira,^a Kalil Z. R. de Sousa,^a Wagner L. Massarotto,^a Emiliane G. Ricci,^a Emerson H. de Faria,^a Katia J. Ciuffi,^{✉a} Dragutin Sevic,^b Lucas A. Rocha^a and Eduardo J. Nassar^{✉*,a}

^aDepartamento de Química, Universidade de Franca, Av. Dr. Armando Salles Oliveira, 201, Pq. Universitário, 14404-600 Franca-SP, Brazil

^bLaboratory for Atomic Collision Processes, Institute of Physics, University of Belgrade, Pregrevica 118, P.O. Box 68, 11080 Belgrade, Serbia

The properties of lanthanides allow them to be used as contrast agents for magnetic resonance imaging, thereby helping to differentiate between tissues, organs, and pathologies more efficiently. Lanthanides contain thermosensitive energy levels that aid identification of cancer and healthy cells. This work investigates the GdVO₄ matrix obtained by the non-hydrolytic sol-gel methodology and doped with the lanthanide ions Er³⁺ and Yb³⁺ at a 1:1 molar ratio. The efficiency of the optical parameters was analyzed on the basis of the Er³⁺ green emission after excitation in the infrared region, namely 980 nm. The temperature-dependent fluorescence intensity ratio (FIR) between the thermally coupled Er³⁺ levels (²H_{11/2} and ⁴S_{3/2} → ⁴I_{15/2}) was evaluated. The Er³⁺ emission depended on the laser power. The calculated number of photons was 2 in this case. Temperatures ranging from 298.3 to 374.5 K were assessed, and the sensitivity varied from 1.2 to 1.9% K⁻¹, respectively. The initial temperature was estimated.

Keywords: biomedical applications, sensitivity, FIR, thermal coupled level

Introduction

Over the last decades, technological advances have provided improved image definition for more precise diagnoses and have allowed diseases to be treated more efficiently. This technological progress has increased the life expectancy of the world population. In many cases, a single method may not meet the necessary requirements for a definitive diagnosis due to factors such as low sensitivity, low penetration into the affected tissue, and overlapping signals, among others. To facilitate medical diagnosis, imaging techniques can be combined, and materials that can respond to different stimuli, like magnetic field, photostimulation (fluorescence), and temperature, can be used.

Cancer and healthy cells have distinct temperatures. Therefore, distinction between these cells requires that the temperature of biological systems be monitored.¹ Systems known as nanothermometers contain nanoparticles and can be employed to measure temperatures at the molecular

level. The ability of nanosensors to measure the temperature depends on the properties of the materials constituting the sensors, including dispersion, particle size, and surface roughness.²

Lanthanide ions have important applications in the medical area: their unique magnetic and photoluminescence properties favor their use in bioimaging.³⁻¹⁰ Different systems can be applied as nanothermometers, mainly systems based on lanthanide ions. The up-conversion mechanism is appropriate for temperature sensors—excitation that occurs in the near infrared, the region of the biological window, thereby increasing penetration into the skin. The lanthanide elements present thermosensitive energy levels, that is, the intensity of the emission depends on temperature. The lanthanides Eu³⁺ and Tb³⁺ exhibit excitation lines, especially in the ultraviolet region, but they can also be employed in up-conversion systems.¹ In turn, Er³⁺, Tm³⁺, and Nd³⁺ can be excited in the near infrared (biological window). Table 1 lists the sensitivity, temperature range, and corresponding references of some systems based on Er³⁺ and Yb³⁺.

*e-mail: eduardo.nassar@unifran.edu.br

Table 1. Optical parameters based on the luminescence of Er³⁺

System	Sensitivity / (% K ⁻¹)	Temperature range / K	Reference
NaGd(WO ₄) ₂ :Yb ³⁺ /Er ³⁺	1.20	310	11
NaGdTiO ₂ :Yb ³⁺ /Er ³⁺	0.83	100-1000	12
NaY(MoO ₄) ₁₂ :Yb ³⁺ /Er ³⁺	0.97	303-523	13
SrWO ₄ :Yb ³⁺ /Er ³⁺	1.10	299-518	14
CaF ₂ :Yb ³⁺ /Er ³⁺	1.40	295-723	15
Ca _{1-x} Na _x MoO ₄ :Yb ³⁺ /Er ³⁺	1.42	336.2-536.2	16
NaLuF ₄ :Yb ³⁺ /Er ³⁺	1.94	296-420	17
SrBi ₄ Ti ₄ O ₁₅ :Er ³⁺ /Yb ³⁺	0.36	313-573	18
LiNbO ₃ :Er ³⁺ /Yb ³⁺	0.75	285-455	19
CeO ₂ :Yb ₃ Er ₂	0.30	148-284	20
GdVO ₄ @SiO ₂ :Er ³⁺ /Yb ³⁺	1.01	297-343	21
GdVO ₄ :Er ³⁺ /Yb ³⁺	0.69	297-343	21
BaTiO ₃ :Er ³⁺	0.52	322-466	22
NaYF ₄ :Er ³⁺ /Yb ³⁺	0.50	298-333	23
NaY(WO ₄) ₂ :Er ³⁺	1.82	293-518	24
LuVO ₄ :Er ³⁺ /Yb ³⁺	0.67	100-500	25

In this study, we have prepared a GdVO₄ matrix by the non-hydrolytic sol-gel methodology and doped it with Er³⁺ and Yb³⁺ at a 1:1 molar ratio (Gd_{0.98}VO₄Er_{0.01}³⁺Yb_{0.01}³⁺). Then, we characterized the systems by X-ray diffraction, infrared spectroscopy, UV-Vis absorption, and photoluminescence. Finally, we analyzed the optical parameters to verify whether the doped matrix is suitable for application as temperature sensor.

Experimental

Lanthanides and vanadium solutions

The lanthanide oxides (Gd₂O₃, Er₂O₃, and Yb₂O₃) were dissolved in HCl (6.0 mol L⁻¹) to obtain a final concentration of 0.1 mol L⁻¹. VCl₅ was prepared by dissolution of V₂O₅. All the reagents were purchased from Sigma-Aldrich Brazil Ltda (São Paulo, Brazil).

Obtention of GdVO₄:Er³⁺, Yb³⁺

The non-hydrolytic sol-gel route has been described by Acosta *et al.*²⁶ The methodology has been modified by Ciuffi *et al.*²⁷ and employed in our laboratory.

The non-hydrolytic process was carried out in oven-dried glassware. The oxide matrix was prepared from the metal chloride under dry conditions and inert atmosphere. The ethanolic solutions of the precursors (GdCl₃, ErCl₃, YbCl₃, and VCl₅) were mixed and heated at 110 °C for 4 h,

under stirring. The resulting solution was cooled to room temperature and aged for 24 h; the solvent was removed; and the final product (powder) was treated at 800 °C for 4 h.

The sample was characterized by powder X-ray diffraction on a Rigaku MiniFlex II diffractometer operating at 30 kV and 15 mA with Cu K α radiation. The Fourier transform infrared (FTIR) spectra were recorded from 4000 to 400 cm⁻¹ (attenuated total reflection (ATR) mode) on a PerkinElmer Frontier spectrophotometer. The solid UV-Vis spectra were obtained on the Ocean Optics spectrometer; magnesium oxide was employed as standard, and the measurement was conducted by using diffuse reflectance, a PX-2 pulsed xenon light source, and a QE65000 Ocean Optics detector. Photoluminescence up-conversion (UC) was registered on a Horiba Jobin Yvon Fluorolog-3 spectrofluorimeter equipped with a double monochromator and a R 928 Hamamatsu photomultiplier. A laser excitation at 980 nm was used for the up-conversion measurements.

Results and Discussion

X-ray diffraction (XRD)

Figure 1 shows the XRD pattern of the GdVO₄:Er³⁺/Yb³⁺ matrix obtained by the non-hydrolytic sol-gel methodology. The peaks agreed with the standard data in JCPDS No. 17-260. There were no peaks related to impurity, which indicated that the product consisted of pure tetragonal gadolinium vanadium oxide with space group I41/amd

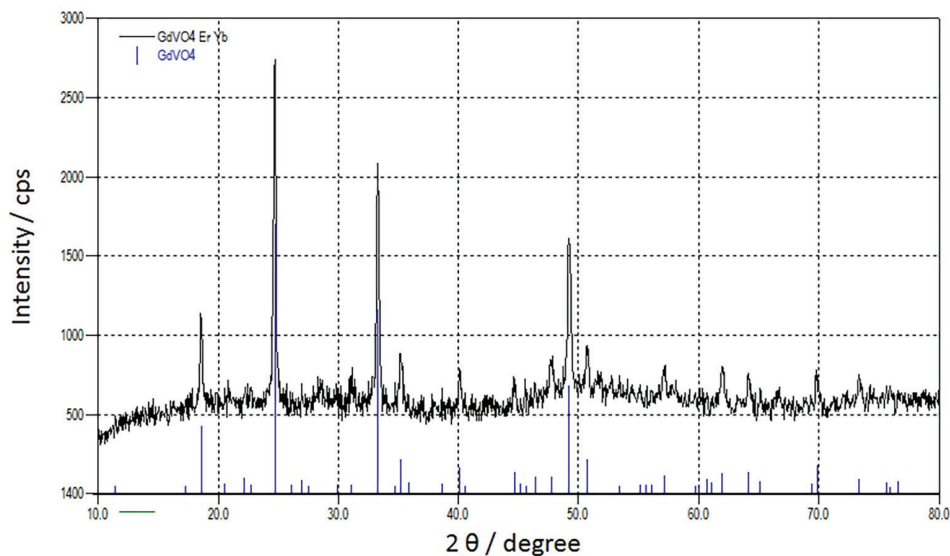


Figure 1. X-ray diffraction patterns of the GdVO₄:Er³⁺/Yb³⁺ matrix with standard JCPDS No. 17-260 for tetragonal phase.

(No. 141). Gavrilović *et al.*²⁸ obtained the same results when they synthesized the matrix by the reverse micelle method. The XRD pattern revealed that the matrix lattice did not affect the dopant ions, which were successfully incorporated and occupied the Gd³⁺ sites.

We estimated the average crystallite sizes from the diffraction peaks by using the Scherrer method.²⁹ This method considers that the crystallite is spherical, so the geometric factor is close to one. Therefore, we considered that the particle was spherical and used this same factor. The calculated crystallite size was 33.4 nm. This result was compatible with the value obtained by our group for the synthesis of the YVO₄ matrix doped with Eu³⁺: around 50 nm.³⁰⁻³³ The ionic radii of the lanthanides present in the GdVO₄:Er³⁺/Yb³⁺ matrix are very similar: $r = 0.94, 0.89,$ and 0.87 \AA for Gd³⁺, Er³⁺, and Yb³⁺, respectively, so the lattice was not distorted.

Infrared spectra (FTIR)

The infrared spectra of the GdVO₄:Er³⁺/Yb³⁺ matrix prepared by the non-hydrolytic sol-gel methodology and treated at 800 °C for 4 h was typical of VO₄³⁻, with peaks at 873 and 814 cm⁻¹. Bands in the ranges of 3000-3500 and 1100-1650 cm⁻¹ corresponded to C-H and O-H stretching of the residual precursors. The band at 451 cm⁻¹ referred to Gd-O.³⁴⁻³⁹ The infrared spectra is in the Supplementary Information (SI) section, Figure S1.

Solid UV-Vis-NIR

Figure 2 illustrates the absorption spectra of the GdVO₄:Er³⁺/Yb³⁺ matrix recorded from 200 to 1000 nm.

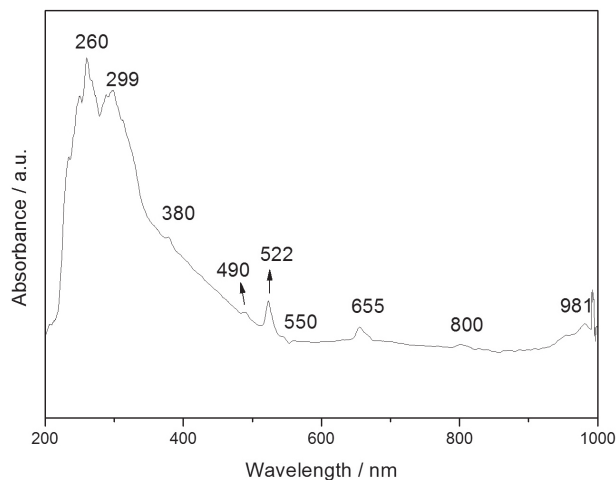


Figure 2. UV-Vis-NIR absorption spectra of the GdVO₄:Er³⁺/Yb³⁺ matrix.

Figure 2 displays the characteristic absorption bands of the lanthanide ions. Table 2 depicts the Er³⁺ and Yb³⁺ absorption wavelengths. The Er³⁺ absorption bands appeared in the UV-Vis-NIR regions. As for Yb³⁺, the absorption band emerged around 980 nm and corresponded to the excited state ²F_{5/2}, which overlapped with the Er³⁺ ⁴I_{11/2} level. The difference between the thermally couple levels (²H_{11/2} and ⁴S_{3/2}) was obtained from the UV-Vis-NIR absorption spectra of the matrix ($\Delta E = 928 \text{ cm}^{-1}$).

The Gd³⁺ energy levels are located in the UV spectral region (below 312 nm), which opens opportunities to convert UV radiation into visible light due to the resonant energy levels between Gd³⁺ and Er³⁺ ions. In fact, this can initially occur from Gd³⁺ excitation (⁸S_{7/2} → ⁶I_{3/2} and ⁶P_J transitions). Then, energy is transferred from these levels to the ²P_J levels of Er³⁺ ions, followed by a non-radiative decay to the ⁴S_{3/2} level and subsequent emission

Table 2. Absorption bands of the energy levels of lanthanide ions in the UV-Vis-NIR spectra of the GdVO₄:Er³⁺/Yb³⁺ matrix from the ground state of Er³⁺ (⁴I_{15/2}) and Yb³⁺ (²F_{7/2})

Energy level	⁴ G _{11/2} (Er ³⁺)	² H _{9/2} (Er ³⁺)	² F _{3/2} , ² F _{5/2} (Er ³⁺)	⁴ F _{7/2} (Er ³⁺)	² H _{11/2} (Er ³⁺)	⁴ S _{3/2} (Er ³⁺)	⁴ F _{9/2} (Er ³⁺)	⁴ I _{9/2} (Er ³⁺)	⁴ I _{11/2} (Er ³⁺)	² F _{5/2} (Yb ³⁺)
Wavelength / nm	380	410	450	490	522	550	650	800	981	

in the visible range.³⁹⁻⁴¹ The broad band between 221 and 353 nm corresponded to the O²⁻ → V⁵⁺ absorption and to the O²⁻ → Ln³⁺ charge transfer band (CTB), as described in the literature,^{28,30-33,42-44} the excitation spectra confirm the CTB (Figure S2, SI section).

Photoluminescence (PL)

We calculated the optical parameters by the equation described in the literature.^{45,46} The fluorescence intensity ratio (FIR) is a methodology that helps to determine the temperature by measuring the fluorescence intensity due to two thermally coupled energy levels in Er³⁺ ions:

$$\text{FIR} = \frac{I_1}{I_2} = A \exp\left(\frac{-\Delta E}{kT}\right) \quad (1)$$

where ΔE is the difference in energy between Er³⁺ ²H_{11/2} and ⁴S_{3/2}, k is the Boltzmann constant, T is the absolute temperature, and A is an experimental constant that depends on the system.

Equation 1 can be rewritten as:

$$\ln(\text{FIR}) = \ln(A) - \frac{\Delta E}{kT} \quad (2)$$

Therefore, the temperature of the system can be calculated by using equation 3.

$$T = \left(\frac{1}{\ln A - \ln(\text{FIR})} \right) \frac{\Delta E}{k} \quad (3)$$

The population redistribution ability (PRA) is another parameter that can be obtained from the emission spectra of lanthanide ions and thus help to determine their application as nanothermometer. PRA can be estimated by equation 4.⁴⁷

$$\text{PRA} = \frac{A}{A + \exp(\Delta E / kT)} \quad (4)$$

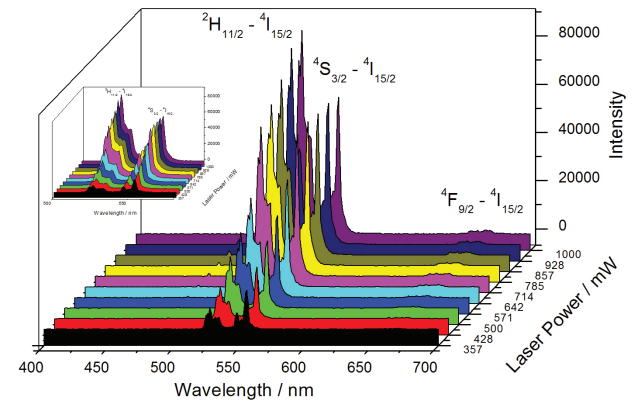
The absolute (S) and the relative (S_R) thermal sensitivities are parameters that indicate the thermometric capacity and can be obtained by equations 5 and 6, respectively.⁴⁸

$$S = \frac{d(\text{FIR})}{dT} = \text{FIR} \frac{\Delta E}{kT^2} \quad (5)$$

$$S_R = \frac{1}{\text{FIR}} \frac{d(\text{FIR})}{dT} = \frac{\Delta E}{kT^2} \quad (6)$$

Information about temperature changes obtained for systems doped with lanthanide ions determines the use of these systems in the industrial and medical fields.

Figure 3 contains the Er³⁺ emission spectrum after excitation at 980 nm with different laser powers.

**Figure 3.** Emission spectra of Er³⁺ doped into GdVO₄, excited at 980 nm, as a function of the laser power, detail of the green region (500 to 600 nm).

The emission spectrum (Figure 3) presented the characteristic Er³⁺ bands. The most intense band emerged in the green region and corresponded to the ²H_{11/2} → ⁴I_{15/2} (524 nm) and ⁴S_{3/2} → ⁴I_{15/2} (555 nm) transitions. A very weak emission arose in the red region and was attributed to the ⁴F_{9/2} → ⁴I_{15/2} transition (660 nm). The detail of the green region showed that the intensity of the emission depended on the laser power: the intensity increased up to 642 mW; thereafter, the area of the ⁴S_{3/2} → ⁴I_{15/2} (555 nm) transition did not change with the laser power because of the thermal excitation to the ²H_{11/2} level. Figure 4 shows how the areas of the transitions ²H_{11/2} → ⁴I_{15/2} and ⁴S_{3/2} → ⁴I_{15/2} depended on the laser power.

Until 642 mW, the intensity of the transitions in the green region increased linearly. In Figure 4, the emission at 555 nm clearly stabilized after 714 mW. For this same laser power, the area of the emission at 524 nm increased more slowly, which could be ascribed to thermal excitation from the ⁴S_{3/2} to the ²H_{11/2} level. The diagram in Figure 5

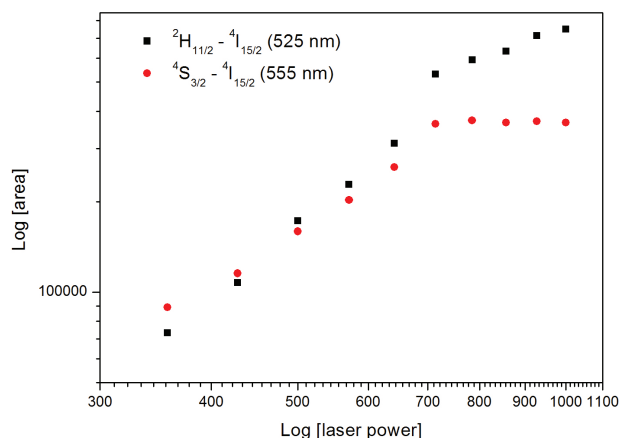


Figure 4. Relationship between the log area of the band and the log laser power: (square) ${}^2H_{11/2} \rightarrow {}^4I_{15/2}$ (524 nm) and (circle) ${}^4S_{3/2} \rightarrow {}^4I_{15/2}$ (555 nm) transitions.

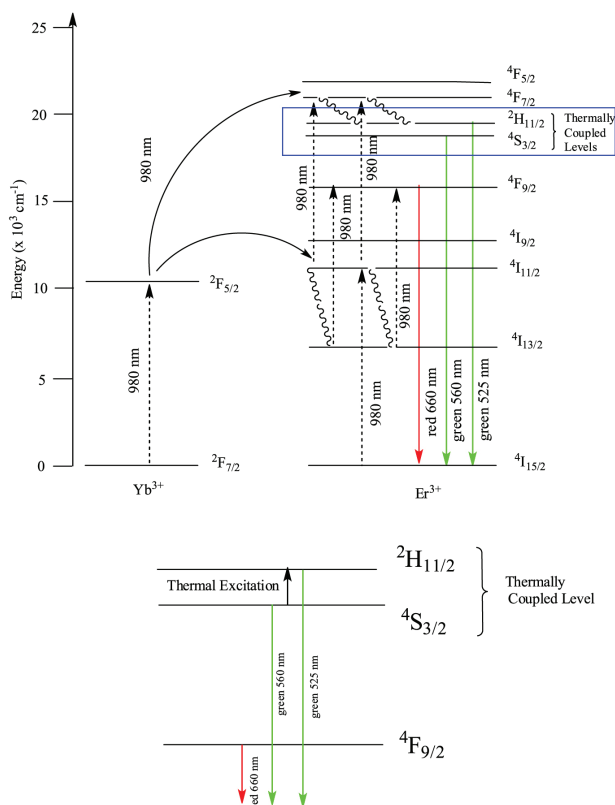


Figure 5. Energy level diagrams for Er³⁺ and Yb³⁺, detail of the thermally coupled level.

represents the excitation and the emission mechanisms of the Er³⁺/Yb³⁺ pair in the GdVO₄ matrix.

The up-conversion mechanisms related to the green emissions can be obtained by the integrated area (IA) of the band corresponding to the ${}^2H_{11/2} \rightarrow {}^4I_{15/2}$ and ${}^4S_{3/2} \rightarrow {}^4I_{15/2}$ transitions as a function of the laser power (LP). The number of absorbed infrared photons *per* emitted visible photon can be determined from the slope of the linear fit of log (IA) vs. log (LP).^{46,49} The linear adjustment

with the experimental data obtained for the sample (linearity, $R > 0.99$) and the average number of photons involved in the process were 2.49 and 1.84 for 525 and 555 nm, respectively. The lower value indicated that the temperature affected the Er³⁺ ion thermally coupled level, as a result of the power laser that was applied to excite the sample.

Figure 6 shows how the FIR depends on the laser power from 357 to 1000 mW.

On the basis of Figure 6, the FIR increased as a function of the laser power, which pointed out that the local temperature augmented. This result demonstrated that the GdVO₄:Er³⁺/Yb³⁺ matrix was sensitive to temperature and could be applied as sensor. Equation 1 shows how the FIR was related to temperature: this relationship depended on A, which is an experimental constant of the system and can be calculated if the initial temperature is considered as 298 K (room temperature). Therefore, by using equation 3, the temperatures of the spectra obtained with different laser powers were determined. The FIR values were obtained from experimental results. Figure 7 illustrates how the Er³⁺ green emission varied with temperature.

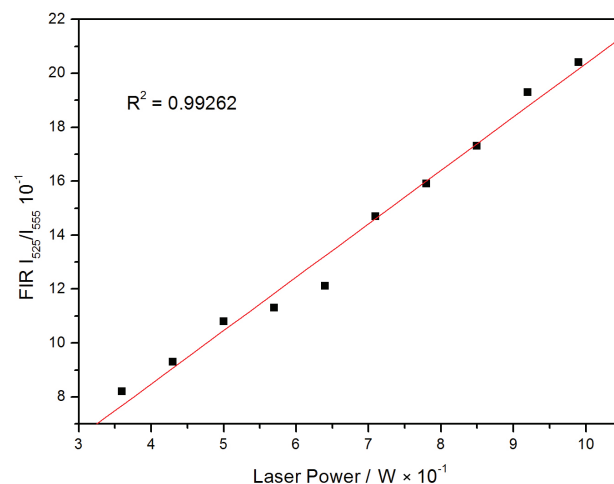


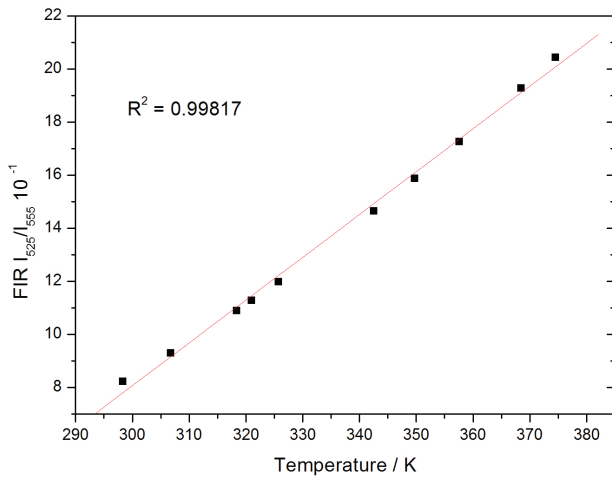
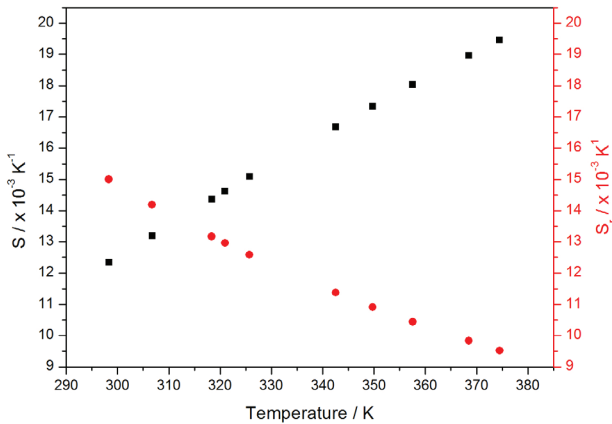
Figure 6. FIR as a function of the laser power.

Figure 7 depicts the linear adjustment with the experimental data for the GdVO₄:Er³⁺/Yb³⁺ matrix FIR values *versus* the calculated temperature. R was 0.99817, so the system provided good results for applications at temperatures ranging from 298 to 374 K (25 to 100 °C). This range agreed with several systems presented in Table 1 and confirmed the results obtained in Figure 6.

The absolute (S) and the relative (S_R) thermal sensitivities can also be used to evaluate whether a material has potential applications in optical thermometry. S and S_R can be calculated by equations 5 and 6. Figure 8 shows the parameters S and S_R .

Table 3. Absolute (S) and relative (S_R) thermal sensitivities based on $GdVO_4:Er^{3+}$ and $GdVO_4:Er^{3+}/Yb^{3+}$ at different lanthanide concentrations

Matrix	Er ³⁺ / %	Yb ³⁺ / %	S (temperature / K) / (% K ⁻¹)	S _R (temperature / K) / (% K ⁻¹)	Reference
GdVO ₄	2	–	7.26 (440)	1.08 (300)	36
	2	8	11.04 (450)	1.34 (300)	36
	1	20	12.56 (453)	1.20 (303)	36
	1	8	7.70 (450)	1.17 (300)	36
	2	10	8.50	1.11 (307)	28
	1	1	1.60	1.20	this work

**Figure 7.** Er³⁺ green emission dependence on temperature for the $GdVO_4:Er^{3+}/Yb^{3+}$ matrix excited at 980 nm.**Figure 8.** Absolute (circle) and relative (square) sensitivities of the $GdVO_4:Er^{3+}/Yb^{3+}$ matrix as a function of temperature.

S and S_R are employed to compare different systems for application as optical sensors. Equation 6 shows how S_R depends on the FIR: increasing FIR augments the difference in energy between thermally coupled levels, which in turn depends on the crystal field and hence on the matrix. This difference in energy levels provides the system with higher sensitivity. S_R does not depend on the matrix nature (mechanical, electrical, and optical properties). S and S_R are expressed in units of percent change *per* Kelvin degree.^{46,50}

In this work, S ranged from 1.23 to 1.95% K⁻¹. According to the linear adjustment displayed in Figure 8, these values reflected how the matrix influenced the sensitivity of the material (see Table 1 and the literature).² We did not observe S_{max} for the studied temperature range. S_R also presented linear adjustment. Its value did not depend on the nature of the thermometer, so the FIR parameter was not considered in equation 6. The decrease in S_R (Figure 8) indicated that this parameter only depended on temperature. S_R did not affect the energy difference between the thermally coupled levels (ΔE).

For the $GdVO_4:Er^{3+}/Yb^{3+}$ system, the S and S_R values reported in the literature depended on lanthanide concentration (Table 3).

In the present case, doping the $GdVO_4$ matrix obtained by the non-hydrolytic sol-gel methodology with 1% Er³⁺ and Yb³⁺ afforded $S = 1.60$ and $S_R = 1.20\%$ K⁻¹ for temperatures ranging from 298 to 374 K. These results indicated that the system can be applied as optical thermometer. When we compared how the lanthanide substitute in the vanadate ion impacted the investigated properties, we found that Y³⁺, Gd³⁺, and Lu³⁺ gave similar S values and temperature range (Table 4).

Table 4. Absolute sensitivity (S) and temperature range for different lanthanide ions (Y³⁺, Gd³⁺, and Lu³⁺) in the vanadate matrix

Matrix	S / (% K ⁻¹)	Temperature range / K	Reference
YVO ₄ :Er ³⁺ /Yb ³⁺	1.17	300-485	51
GdVO ₄ :Er ³⁺ /Yb ³⁺	0.85	307-473	28
LuVO ₄ :Er ³⁺ /Yb ³⁺	0.67	100-500	25
GdVO ₄ :Er ³⁺ :Yb ³⁺	1.60	298-374	this work

Equation 4 can be employed to calculate the dependence of the population redistribution ability (PRA) of the ²H_{11/2} and ⁴S_{3/2} thermally coupled levels on temperature (see Figure 9).

Figure 9 clearly shows that temperature affected the PRA value. At 298 K, the PRA was low (0.45), whereas

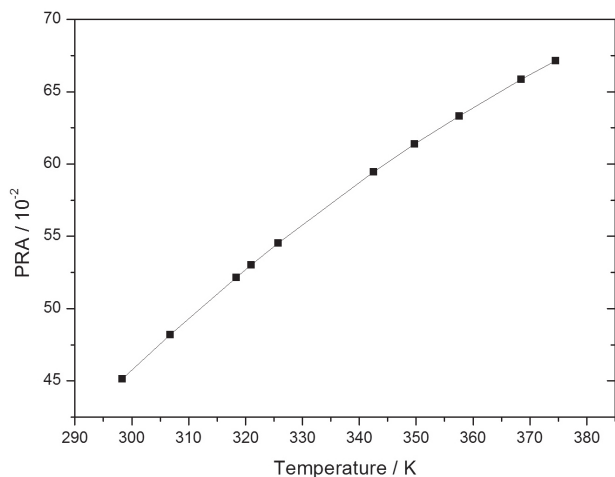


Figure 9. PRA as a function of temperature.

at 374 K, the maximum temperature tested in this work, the PRA increased (0.67). These results suggested that temperature affected the population between thermally coupled levels, which is a satisfactory behavior for non-contact nanothermometers based on the FIR. Du *et al.*⁴⁷ achieved similar results for the NaBiF₄ system: the PRA varied from 0.22 to 0.54 for temperatures between 300 and 483 K, respectively.

We measured the photoluminescence of the GdVO₄:Er³⁺/Yb³⁺ matrix at fixed laser powers of 357 and 714 mW and varied the time between the spectra. Figure S3 (SI section) contains the emission spectra excited at 980 nm with two-minute interval between the measurements. The spectra were recorded every one minute.

The emission spectra displayed the typical Er³⁺ bands. The bands in the green region, at 525 and 555 nm, corresponded to the ²H_{11/2} → ⁴I_{15/2} and ⁴S_{3/2} → ⁴I_{15/2} transitions, respectively. The band in the red region, at 650 nm, was attributed to the ⁴F_{9/2} → ⁴I_{15/2} transition. The spectra recorded at different times (one-minute interval) overlapped, which indicated that the local temperature of the sample returned to room temperature after 1 min. Figure 10 shows the integral area of the bands in the green region (525 and 555 nm) as a function of time between the excitations. The inset details the FIR for laser powers of 357 and 714 mW.

On the basis of Figure 10, the integral area of the ²H_{11/2} → ⁴I_{15/2} and ⁴S_{3/2} → ⁴I_{15/2} transitions upon excitation at 980 nm were higher for the laser power of 714 mW as compared to the laser power of 357 mW, as observed in Figure 4. The area did not change considerably as a function of time; i.e., the one-minute interval allowed between the recorded spectra. This suggested that the GdVO₄ matrix exhibited good heat dissipation property. According to the inset in Figure 10, the temperature did not modify the FIR as function of time for any of the two laser powers.

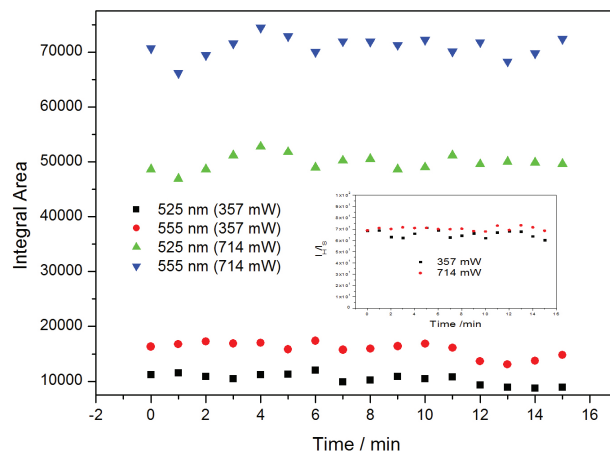


Figure 10. Integral area of the band at 525 and 555 nm corresponding to the ²H_{11/2} → ⁴I_{15/2} and ⁴S_{3/2} → ⁴I_{15/2} transitions, respectively, after excitation at 980 nm with laser power of 357 or 714 mW as a function of time. The inset details the FIR as a function of time.

In the case of continuous measurements, as shown in Figure 3, the local temperature increased due to constant exposure of the sample to the laser. When a one-minute interval was allowed between the measurements, the temperature did not rise. Therefore, one minute was enough for the sample to cool.

Conclusions

A GdVO₄ matrix doped with the lanthanides Er³⁺ and Yb³⁺ can be prepared by the non-hydrolytic sol-gel methodology. The XRD and infrared techniques confirmed the structure of the matrix. The UV-Vis-NIR absorption spectrum indicated that the matrix is indeed doped with Er³⁺ and Yb³⁺.

Upconversion of the luminescence properties of the lanthanides revealed energy transfer from Yb³⁺ to Er³⁺ upon excitation at 980 nm. The Er³⁺ emission corresponds to a strong band in the green region. Two photons had to be absorbed for Er³⁺ excitation.

The system depends on temperature, mainly with respect to the heating promoted by the laser power. When one minute is allowed between measurements, the temperature does not increase, but it remains constant.

In summary, the emission properties of the lanthanides doped into the GdVO₄ matrix depends on temperature, which paves the way for several applications such as contrast agents for magnetic resonance imaging and thermometer medical sensors, to help differentiate between tissues, organs, and pathologies.

Supplementary Information

Supplementary data (infrared, excitation, and emission)

are available free of charge at <http://jbcs.sbq.org.br> as PDF file.

Acknowledgments

Part of this study was funded by Coordenação de Aperfeiçoamento de Pessoal de Nível Superior-Brazil (CAPES), finance code 001. São Paulo Research Foundation (FAPESP, grant 2015/20298-0 L.A.R and 2019/02641-0 E.J.N.), Conselho Nacional de Desenvolvimento Científico e Tecnológico (CNPq, grant 302702/2018-0 L.A.R. and 302668/2017-9 E.J.N.) are also acknowledged. The author from Serbia acknowledges funding provided by the Institute of Physics Belgrade, through the grant by the Ministry of Education, Science, and Technological Development of the Republic of Serbia.

Author Contributions

M. F. F., K. Z. R. S., W. L. M. were responsible for study design and data collection; E. G. R., E. H. F., K. J. C. for statistical analysis and data interpretation; D. S., L. A. R., E. J. N. for manuscript preparation, literature search, and funds collection.

References

- Brites, C. D. S.; Lima, P. P.; Silva, N. J. O.; Millán, A.; Amaral, V. S.; Palacio, F.; Carlos, L. D.; *Adv. Mater.* **2010**, *22*, 4499.
- Brites, C. D. S.; Lima, P. P.; Silva, N. J. O.; Millan, A.; Amaral, V. S.; Palacio, F.; Carlos, L. D.; *Nanoscale* **2012**, *4*, 4799.
- Chen, B.; Zhang, H.; Du, N.; Zhang, B.; Wu, Y.; Shi, D.; Yang, D.; *J. Colloid Interface Sci.* **2012**, *367*, 61.
- Yan, K.; Li, H.; Li, P.; Zhu, H.; Shen, J.; Yi, C.; Wu, S.; Yeung, K. W. K.; Xu, Z.; Xu, H.; Chu, P. K.; *Biomaterials* **2014**, *35*, 344.
- Raju, G. S. R.; Pavitra, E.; Lee, H.; Nagaraju, G.; Baskaran, R.; Yang, S. G.; Kwak, C. H.; Nagaraju, G. P.; Huh, Y. S.; Han, Y.-K.; Ouzo, P.; *Appl. Surf. Sci.* **2020**, *505*, 144584.
- Nassar, E. J.; Moscardini, S. B.; Lechevallier, S.; Vereslt, M.; Borak, B.; Rocha, L. A.; *J. Sol-Gel Sci. Technol.* **2020**, *93*, 546.
- Xu, J.; Gulzar, A.; Yang, P.; Bi, H.; Yang, D.; Gai, S.; He, F.; Lin, J.; Xing, B.; Jin, D.; *Coord. Chem. Rev.* **2019**, *381*, 104.
- Tu, D.; Zheng, W.; Liu, Y.; Zhu, H.; Chen, X.; *Coord. Chem. Rev.* **2014**, *273-274*, 13.
- Zhao, J.; Chen, J.; Ma, S.; Liu, Q.; Huang, L.; Chen, X.; Lou, K.; Wang, W.; *Acta Pharm. Sin. B* **2018**, *8*, 320.
- Wang, Y.; Song, S.; Zhang, S.; Zhang, H.; *Nano Today* **2019**, *25*, 38.
- Yuan, N.; Liu, D.-Y.; Yu, X.-C.; Sun, H.-X.; Ming, C.-G.; Wonga, W.-H.; Song, F.; Yu, D.-Y.; Pun, E. Y.-B.; Zhang, D.-L.; *Mater. Lett.* **2018**, *218*, 337.
- Li, X. P.; Wang, X.; Zhong, H.; Cheng, L. H.; Xu, S.; Sun, J. S.; Zhang, J. S.; Li, X. J.; Tong, L. L.; Chen, B. J.; *Ceram. Int.* **2016**, *42*, 14710.
- Yang, X. X.; Fu, Z. L.; Yang, Y. M.; Zhang, C. P.; Wu, Z. J.; Sheng, T. Q.; *J. Am. Ceram. Soc.* **2015**, *98*, 2595.
- Pandey, A.; Rai, V. K.; Kumar, V.; Kumar, V.; Swart, H. C.; *Sens. Actuators, B* **2015**, *209*, 352.
- Cai, J. J.; Wei, X. T.; Hu, F. F.; Cao, Z. M.; Zhao, L.; Chen, Y. H.; Duan, C. K.; Yin, M.; *Ceram. Int.* **2016**, *42*, 13990.
- Pang, T.; Wan, W.; Qian, D.; Liu, Z.; *J. Alloys Compd.* **2019**, *771*, 571.
- Xu, W.; Chen, Z.; Sun, J.; Xu, J.; Hao, H.; Li, D.; Song, Y.; Wang, Y.; Zhang, X.; *J. Alloys Compd.* **2018**, *766*, 305.
- Wei, T.; Yang, F.; Jing, Q.; Zhao, C.; Wang, M.; Du, M.; Guo, Y.; Zhou, Q.; Li, Z.; *J. Alloys Compd.* **2019**, *801*, 1.
- Quintanilla, M.; Cantelar, E.; Cussó, F.; Villegas, M.; Caballero, A. C.; *Appl. Phys. Express* **2011**, *4*, 022601.
- Baca, L.; Steiner, H.; Stelzer, N.; *J. Alloys Compd.* **2019**, *774*, 418.
- Oleksandr, A.; Savchuk, J. J.; Carvajal, C.; Cascales, M.; Aguilo, M.; Díaz, F.; *ACS Appl. Mater. Interfaces* **2016**, *8*, 7266.
- Alencar, M. A. R. C.; Maciel, G. S.; de Araújo, C. B.; *Appl. Phys. Lett.* **2004**, *84*, 4753.
- Savchuk, O. A.; Carvajal, J. J.; Massons, J.; Cascales, C.; Aguiló, M.; Díaz, F.; *Sens. Actuators, A* **2016**, *250*, 87.
- Zheng, H.; Chen, B.; Yu, H.; Zhang, J.; Sun, J.; Li, X.; Sun, M.; Tian, B.; Zhong, H.; Fu, S.; Hua, R.; Xia, H.; *RSC Adv.* **2014**, *4*, 47556.
- Wu, J.; Cheng, X.; Jiang, F.; Feng, X.; Huang, Q.; Lin, Q.; *Phys. B* **2019**, *561*, 97.
- Acosta, S.; Corriu, R. J. P.; Leclercq, D.; Lefèvre, P.; Mutin, P. H.; Vious, A.; *J. Non-Cryst. Solids* **1994**, *170*, 234.
- Ciuffi, K. J.; de Lima, O. J.; Sacco, H. C.; Nassar, E. J.; *J. Non-Cryst. Solids* **2012**, *304*, 126.
- Gavrilović, T. V.; Jovanović, D. J.; Lojpur, V.; Dramićanin, M. D.; *Sci. Rep.* **2014**, *4*, 4209.
- Li, J.; Chem, Y.; Yin, Y.; Yao, F.; Yao, K.; *Biomaterials* **2007**, *28*, 781.
- Matos, M. G.; de Faria, E. H.; Rocha, L. A.; Calefi, P. S.; Ciuffi, K. J.; Nassar, E. J.; Sarmiento, V. H. V.; *J. Lumin.* **2014**, *147*, 190.
- Matos, M. G.; de Faria, E. H.; Ciuffi, K. J.; Rocha, L. A.; Nassar, E. J.; Vereslt, M.; *Quim. Nova* **2018**, *41*, 849.
- Saltarelli, M.; Matos, M. G.; de Faria, E. H.; Ciuffi, K. J.; Rocha, L. A.; Nassar, E. J.; *J. Sol-Gel Sci. Technol.* **2015**, *73*, 283.
- Saltarelli, M.; Luz, P. P.; Matos, M. G.; de Faria, E. H.; Ciuffi, K. J.; Calefi, P. S.; Rocha, L. A.; Nassar, E. J.; *J. Fluoresc.* **2012**, *22*, 899.
- Zhang, X.; Chen, T.; Xu, Y.; Jiang, W.; Liu, J.; Xie, Z.; *J. Sol-Gel Sci. Technol.* **2019**, *91*, 127.

35. Miura, B. A.; Ferreira, N. H.; Oliveira, P. F.; de Faria, E. H.; Tavares, D. C.; Rocha, L. A.; Ciuffi, K. J.; Nassar, E. J.; *J. Lumin.* **2015**, *159*, 93.
36. Zhang, H.; Fu, X.; Niu, S.; Sun, G.; Xin, Q.; *J. Solid State Chem.* **2004**, *177*, 2649.
37. Liang, Y.; Ouyang, J.; Wang, H.; Wang, W.; Chui, P.; Sun, K.; *Appl. Surf. Sci.* **2012**, *258*, 3689.
38. Bhiri, N. M.; Dammak, M.; Aguilo, M.; Díaz, F.; Carvajal, J. J.; Pujol, M. C.; *J. Alloys Compd.* **2020**, *814*, 152197.
39. Matos, M. G.; Calefi, P. S.; Ciuffi, K. J.; Nassar, E. J.; *Inorg. Chim. Acta* **2011**, *375*, 63.
40. Oliveira, H. H. S.; Cebim, M. A.; da Silva, A. A.; Davolos, M. R.; *J. Alloys Compd.* **2009**, *488*, 619.
41. Zatsopin, A.; Kuznetsova, Y.; *Appl. Mater. Today* **2018**, *12*, 34.
42. Matos, M. G.; Rocha, L. A.; Nassar, E. J.; Verelst, M.; *Opt. Mater.* **2016**, *62*, 12.
43. Ferreira, M. F.; de Andrade, F. H. P.; Granito, C. J.; Melo, W. E. N.; de Faria, E. H.; Ciuffi, K. J.; Rocha, L. A.; Nassar, E. J.; *J. Fluoresc.* **2020**, *30*, 827.
44. Sevic, D.; Rabasovic, M. S.; Krizan, J.; Savic-Sevic, S.; Nikolic, M. G.; Marinkovic, B. P.; Rabasovic, M. D.; *J. Phys. D: Appl. Phys.* **2020**, *53*, 015106.
45. Wu, Y.; Suo, H.; He, D.; Guo, C.; *Mater. Res. Bull.* **2018**, *106*, 14.
46. Manzani, D.; Petrucci, J. F. S.; Nigoghossian, K.; Cardoso, A. A.; Ribeiro, S. J. L.; *Sci. Rep.* **2017**, *7*, 41596.
47. Du, P.; Luo, L.; Huang, X.; Yu, J. S.; *J. Colloid Interface Sci.* **2018**, *514*, 172.
48. Wu, Y.; Zhang, Z.; Suo, H.; Zhao, X.; Guo, C.; *J. Lumin.* **2019**, *214*, 116578.
49. Yeh, D. C.; Sibley, W. A.; Suscavage, M.; Drexhage, M. G.; *J. Appl. Phys.* **1987**, *62*, 266.
50. Rai, V. K.; *Appl. Phys. B* **2007**, *88*, 297.
51. Mahata, M. K.; Kumar, K.; Rai, V. K.; *Sens. Actuators, B* **2015**, *209*, 775.

Submitted: April 24, 2020

Published online: September 17, 2020

